Spatially Selective, Solid State Etching of Diamond using Lithographically Patterned FeCoB

Zhijie Wang and M. Ravi Shankar*
Department of Industrial Engineering
Swanson School of Engineering
University of Pittsburgh, PA 15261
* ravishm@pitt.edu

Abstract:

Nanocrystalline layers of FeCoB (Fe:Co:B=60:20:20 at atom r atio) enable spatially selective, microstructurally agnostic removal of diamond through a solid-state diffusion reaction. Lithographically fabricated 100-300nm thick films of FeCoB are deposited on polycrystalline diamond substrates. Heat treatment at temperatures ranging from 700℃-900℃ for 30min-90min are used to trigger the conversion of sp^3 to sp^2 carbon at the diamond-transition metal interface. The integrity of the solid-state etchant within the thermal processing window underpins the spatial selectivity with which the diamond is removed. Removal of the reaction products using solvothermal etching in an acid solution enables the recovery of the structured diamond surfaces. FeCoB offers material removal rates, which exceeds that possible with just Fe or Co – pointing to the key role of B. The interaction zone was excised using focused ion beam milling and characterized using electron microscopy. In addition, XRD and Raman spectroscopy were performed to study the phase composition of the interaction zone. The role of the transition metal-diamond interface is key to controlling the material removal; the stability of the interface determines the ability to faithfully replicate the ultrafine features that were lithographically patterned in the FeCoB.

Keywords: diamond, diffusion, etching, interface characterization, surface characterization

1. Introduction:

In addition to its high modulus and hardness, diamond presents unique chemical and optical properties. Its high hardness is a key enabler for breakthroughs in ultraprecision machining [1-3](diamond turning processes) and in enabling a pathway for accessing high pressures in the 100's of GPa range[4] . Its chemical inertness [5], optical stability [6] and biocompatibility [7] have magnified the design space, wherein these functional properties can be exploited. Diamond has found a niche in MEMS [8], optical elements [6], sensors [9-13], and in information processing [14]. Integration of diamond and its patterning to enable these applications poses unique challenges. Existing process schema that harness etching-based methods range from reactive ion etching (RIE) [15, 16], inductively coupled plasma (ICP) [17-19] or electron beam induced etching(EBIE) [20-22]. In addition, laser [23] and focused ion beam (FIB) [24] based machining methods have been utilized to structure diamond. The key focus in such process engineering has been to accelerate material removal and to enable scalability over large areas within a serial production framework [19, 25]. These methods are reliant on fluidic etchants (i.e., plasma, gas, and liquid solution), which place limitations on the geometric complexity that can be endowed. For example, creating a hierarchical structure will require a multistep mask fabrication to fabricate structures in a sequential fashion. More importantly, these etchants require specialized equipment and handling due to their high reactivity, which magnifies the capital costs and limits their scalability for large-volume production.

We are motivated by the ability of d-shell rich transition metals (TM) to rapidly react with

diamond. One manifestation of this is in the rapid deterioration of the cutting tool during diamond turning of metals such as Nb and Fe[26, 27]. This is a highly detrimental feature, which is predominantly driven by graphitization and diffusion [28]. The interaction between d-shell rich TM and diamond results in an intimately bonded "built up edge". This is observed on the single-crystal diamond tool surface (in contact with deformed chip). Furthermore, graphitization is the primary cause of flank wear, where the tool contacts the freshly generated surface. Arrays of microgrooves spontaneously form on the flank side when diamond is used to cut so-called "non-diamond-turnable metals" [29]. Compared with Si, a typical diamond-turnable material, the wear rate is over 100 times higher when cutting non-diamond-turnable materials[27, 30]. The interaction of diamond with d-shell metal plates and powders has also been utilized to polish diamond surfaces [31, 32]. Optimized process designs enable the creation of damage-free diamond surfaces with reduced roughness [31-33]. It has also been shown that crystallographically sensitive etching is possible by exploiting the interaction of diamond with Ni in the presence of water vapor [34]. The advantage of diffusional mass-transport based approaches for patterning is the ability to eschew damage and implantation from the etching sources (e.g., plasma or ion beam) [35-37]. Achieving the ability to pattern and localize the material removal can enable μm and sub-μm scale selectivity in material removal, which is necessary for the creation of optical components from diamond (e.g., gratings and waveplates), especially polycrystalline diamond, which is easier and more economical to be grown into a large dimension (>1 inch) for applications that exploit its functional properties. In such applications, scalable utilization of spatially patterned TM on diamond surfaces with the aim of replicating ultrafine features becomes feasible. With the

availability of an array of compositionally modulated etchants, it is possible to envision site specific patterning of compositionally graded films on diamond, which can replicate hierarchical surface features. However, understanding the process-structure relationships, with a focus on elucidating the underlying mechanisms of mass transport is needed for optimizing this approach.

Here, we study material removal of chemical vapor grown, polycrystalline diamond using FeCoB (Fe:Co:B at 60:20:20 atomic %) patterns on its surface. The focus is on selectively etching μm-scale features in diamond by patterning the TM. Lithography is used to create nanocrystalline FeCoB and is reacted with the underlying diamond via heat treatment at temperatures ranging from 700℃-900℃ for 30min-90min. The effect of time and temperature on the microstructure, composition and phase content is tracked across the diffusion reaction zone using electron microscopy, x-ray diffraction and Raman spectroscopy. The progressive evolution of the microstructure and its effect on the removal of diamond is tracked. Subsequently, the reaction products are removed using solvothermal etching with a mixture of H_2SO_4:HNO_3=3:1 at volume ratio in a reaction chamber. The patterned diamond surfaces are characterized using atomic force microscopy. Within this framework, FeCoB is found to offer accelerated material removal, in comparison to just Fe or Co, and offers a microstructurally agnostic (orientation insensitive) system for patterning diamond.

2. Materials and Methods:

All diamond samples used in this paper are CVD polycrystal samples donated by the II-VI

Corporation. The diamond substrate has a strong texture with preferred orientations close to (101), as shown in Figure S1 (Supplementary Information). Other reagents used in this study include acetone (CH_3COCH_3, ≥ 99.5%), Sulfuric acid (H_2SO_4, 95-98 wt%), and nitric acid (HNO_3, 70 wt%), which were purchased from Fisher Chemicals and used without further purification. The TM are deposited with an electron beam evaporator (FeCoB or Co) or a PVD sputtering system (pure Fe) with 99.9% purity sources that purchased from Kurt J. Lesker Company. The FeCoB source is commercial premixed target with an atomic ratio of Fe:Co:B at 60:20:20. The grain structure of the deposited FeCoB is shown in Figure S2, which indicates that the deposited metal is nanocrystalline with an average grain size of ~20 nm.

2.1. Spatially selective patterning of solid-state etchants: Figure 1(a) illustrates the process scheme. The as received diamond samples were ultrasonically cleaned in acetone for 15 minutes to strip them of surface contaminants. Then, spin coating was used to deposit a photoresist film on the diamond. Subsequently. the photoresist was exposed with an optical maskless aligner (Heidelberg MLA100) to create features with 1μm resolution, followed by development. After that, the diamond sample with the photoresist pattern was placed in an electron beam evaporator (Plassys MEB550S) to deposit FeCoB on top of the sample surfaces. The premixed FeCoB target was evaporated by electron beam (generation HV = 10kV, emission current = 200 ± 10mA) and deposited onto the rotating (5.0 rpm) diamond substrates in a chamber with pressure under 5×10^{-7} mBar. The deposition rate was 0.2 ± 0.01nm/s. After deposition, the photoresist and metals above it were removed using Remover PG (Microchem Solvent Stripper) and isopropyl alcohol (IPA). The metal contacting the diamond was retained.

The obtained samples were then annealed in a vacuum furnace (pumped by Pfeiffer Vacuum D-35614 Asslar TMH 071 P, the maximum remaining pressure during the annealing was 1×10^{-6} mBar) at 700℃, 800℃, and 900℃ for 30 minutes, 60 minutes, and 90 minutes. Finally, the diamond samples were solvothermally cleaned in an acid solution (H_2SO_4:HNO_3=3:1) under 220℃ for 30 minutes to remove the reaction products.

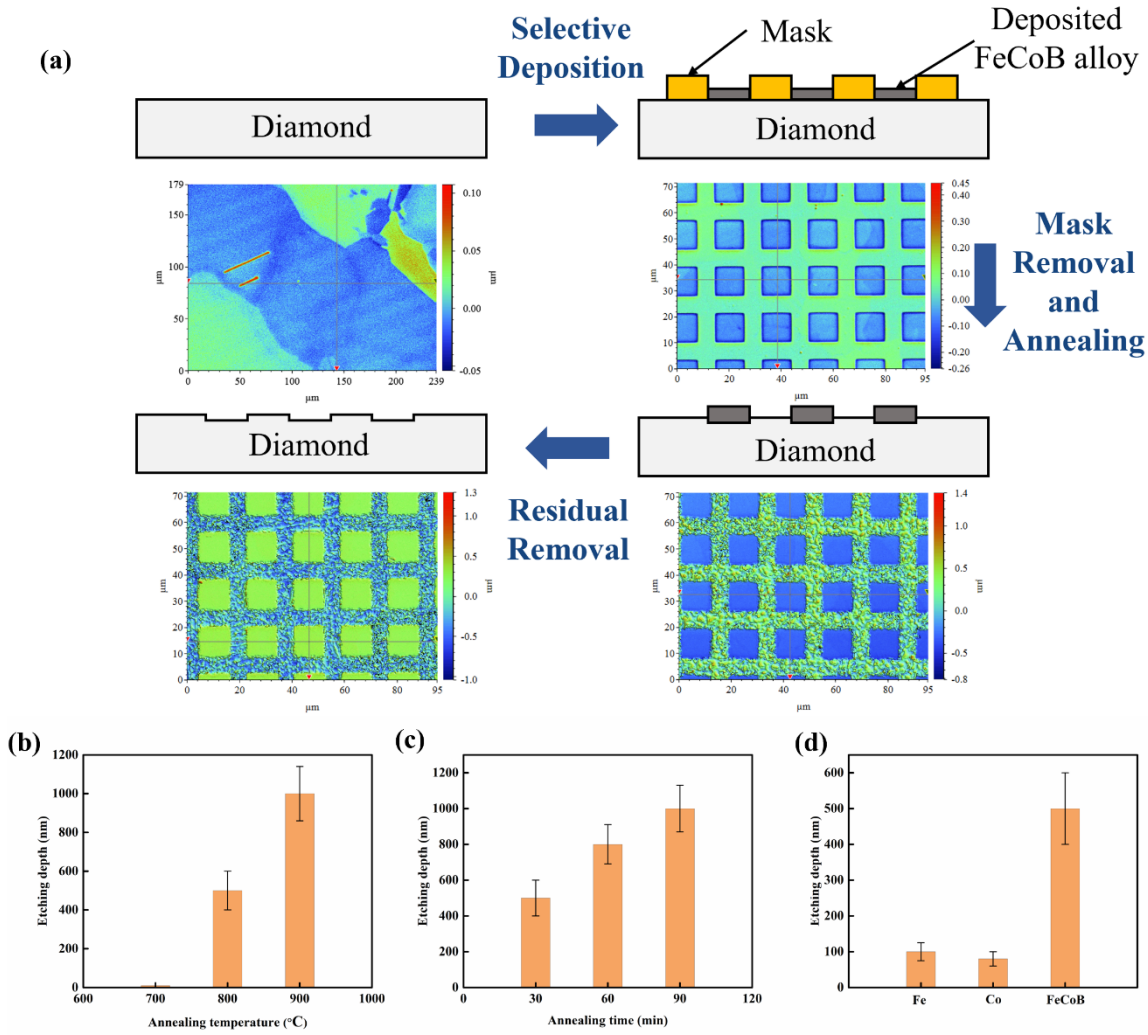

Figure 1 (a) Schematic (cross-section view) showing the process flow to utilize solid state etchants to create patterns on polycrystalline diamond substrate. Optical profilometry was used to characterize

the surface topography (top view) of the substrate surface at each processing step. Note the formation of a stepped topography on diamond at the end of the process. The characterizations shown utilize FeCoB. (b) Etching depth of diamond substrates annealed for 30 min under 700°C, 800°C, 900°C. (c) Etching depth generated at 800°C for 30min, 60min, and 90min. (d) Etching depth with Fe, Co and FeCoB after heat treatment at 800°C for 30min.

2.2. Characterization: Topographies of the samples were measured using an optical profilometer (BRUKER Contour GT-I) and an atomic force microscopy (AFM, BRUKER Dimension Icon). The height of the thin films and the etching depth were measured using the optical profilometer, five scanning was performed at each treatment parameter. The roughness of the patterned or unpatterned area was measured by the AFM, five scanning was performed for each processing condition. The samples were also characterized using a scanning electron microscope (SEM, FEI Apreo) and a transmission electron microscope (TEM, FEI Tecnai G2-F20). The grain orientations of diamond substrates were measured via electron backscattered diffraction (EBSD, FEI Apreo with an EDAX EBSD camera). The composition of the diamond-metal interaction layers was identified via energy-dispersive X-ray spectroscopy (EDS, FEI Apreo with EDAX's Octane SDD), X-ray Diffraction (XRD, Bruker D8), Raman Microscope (Renishaw inVia) and TEM (JEOL JEM-2100F with XEDS detector). The film samples for TEM characterization were extracted from the annealed sample surfaces using a focused ion beam instrument (FIB, FEI Scios DualBeam).

3. Results and discussion:

Figure 1(a) shows the surface profiles corresponding to each process step. It is apparent that the native surface of the as-received diamond samples is reflective of its underlying polycrystalline grain structure (Also, see Supplementary Figure S1). The roughness (Ra) within an individual grain is 3.84 ± 0.47nm, while the overall roughness of the surface is 9.6 ± 1.2nm. The roughness of the deposited FeCoB metal layer (within one diamond grain) is 3.39 ± 0.26nm and the height of the layer is 100 ± 10nm (designed thickness of deposition process ~100nm). After being annealed under 800℃ for 30 minutes, the height of the metal layer increased to 600 ± 100nm and the roughness (Ra) of the surface increased to 224 ± 22nm. The increase in the volume is indicative of the diffusion of carbon atoms into the FeCoB layers during the annealing processes. After solvothermal cleaning, the pattern created using lithography was replicated on the diamond substrate (Figure 1a). The etching depth is 500 ± 100nm, the roughness (Ra) of the etched area is 186 ± 28nm. Figure 1 (b) shows the effect of annealing temperature on the etched depths. Three samples that utilized 100nm thick FeCoB layer were annealed under 700℃, 800℃, and 900℃ respectively. No significant interaction between diamond and FeCoB occurs when the annealing temperature is below 700℃; negligible material removal occurs after the solvothermal treatment. The material removal is accelerated beyond 800℃. The Gibbs free energy change of this reaction $dG < 0$ if the temperature ≥ 800℃. When the temperature reached 900℃, the etching rates are double compared to that at 800℃. However, the profile of the etched area deviates significantly from the pattern of the deposited etchant (FeCoB). This can be seen in the Supplementary Figure S3.

Effect of the reaction time between diamond and FeCoB on the material removal was

explored. Samples consisting of the 100nm FeCoB on the diamond were annealed at 800℃ for 30min, 60min, and 90min, respectively. Figure 1c shows the relationship between the etching depths and annealing time, following the solvothermal treatment. The etching depth increases linearly with time, and the function of the etching depth (h) with respect to the annealing time (t) can be approximately described as $h = kt$, where k is the etching rate that is calculated to 13.5 ± 2.8 nm/min at 800℃ (least squares fit). In addition, the roughness (Ra) of the etched area was measured as a function of reaction time at 800℃. The roughness of the sample annealed for 30min, 60min, and 90min was measured as 186 ± 28nm, 203 ± 26nm, 212 ± 30nm, respectively. The ratio (RD) of etched area roughness to the etching depth is 0.372, 0.254, 0.212, when the etching depth is 500nm, 800nm, and 100nm, respectively. The roughness of the etched area did not increase significantly with the increase of the etching depth. The effect of the thickness of FeCoB on the etching rate was explored. 100nm, 200nm, and 300nm thick FeCoB layers were deposited on diamond and heat treated at 800℃ for 90min. Following the solvothermal treatment, the etched surface was characterized. The thickness of the etched depth (~1000 ± 130 nm) is quite comparable, as illustrated in Figure S4. The independence of the etching rate on the thickness of the deposited metal layer suggests that the key role of these layers is to trigger graphitization and drive C transport away from the interface. The interface of the TM and the diamond is what controls the material removal, given that sp^2 carbon is energetically favorable[38, 39]. The efficacy of FeCoB was compared against that of Fe and Co, which were deposited in a patterned manner on diamond. 100 ± 10nm layers were deposited and the samples were annealed at 800℃ for 30 min. Subsequent topographical characterization showed an etching depth of Fe, Co, and FeCoB of 100 ± 25nm, 80 ± 20nm,

and 500 ± 100nm, respectively (Figure 1d). FeCoB was found to be markedly more efficient at etching diamond than the other systems. The effect of B in accelerating the carbon removal is likely because it can change FeCo alloy crystalline structure, which can increase the carbon diffusion coefficient and reduce activation energy of diamond/TM interaction[40, 41].

The composition of the diffusional interaction layer was analyzed via XRD and Raman spectroscopy, and TEM. Figure 2(a) shows the X-ray diffractograms of the diffusional interaction layer between diamond and 150 ± 10nm FeCoB under 700°C, 800°C, and 900°C for 30min. As can be seen, the major compositions in the diffusional interaction layer are C, FeC, Fe_2C, Fe_3C, Co_3C, B_2C, B_4C, and FeCoB alloy. With increasing annealing temperature, the intensities of these peaks increase. In particular, the peak for C+Co_3C+FeC increases significantly compared other peaks with increasing temperature. This indicates the progressive accumulation of C, Co_3C, and FeC among the reaction products. To further identify the phase structure of the carbon, Raman spectroscopy was performed. As seen in Figure 2(b), the strong G band shows the formation of sp^2 hybridized carbon. The position of the G peak is 1584.84cm^{-1}, which indicates the generated carbon layer contains multilayer graphene[42, 43]. Although the significant D peak indicates high density defects exists in generated sp^2 hybridized carbon[44]. It is unclear if controlling treatment parameters (annealing temperature, annealing time, chemical composition of deposited metal), can enable the creation of high quality graphene on diamond using this approach [42].

TEM analysis was performed to characterize the interaction zone between diamond and

FeCoB. In Figure 2(c), the interface is heterogeneous. Islands of dark contrast are distributed at the boundary of two regions of lower contrast. Carbon due to its low Z value presents a lower contrast. These islands are marked with red arrows. The thickness of the whole reaction zone is approximately 2μm that matches the results of optical profilometery after the heat treatment (Figure 1a). Figure 2 (d) and (e) shows the magnified TEM images of the interaction zone. Dark regions that are likely metal-rich are dispersed in a matrix of lower contrast. The higher resolution imaging of the matrix reveals a crystalline structure with an interplanar spacing of 0.34nm (Figure 2e), which matches that of the XRD peak at 2θ=26.4º (Figure 2a). This is characteristic of that observed in sp^2 carbon[45, 46]. The regions of darker contrast that are dispersed within this matrix are also crystalline and are characterized by a d-spacing of 0.26nm. We were unable to correlate this to a corresponding XRD peak, even though this metal-rich phase presents a strongly diffracting orientation in the TEM micrograph.

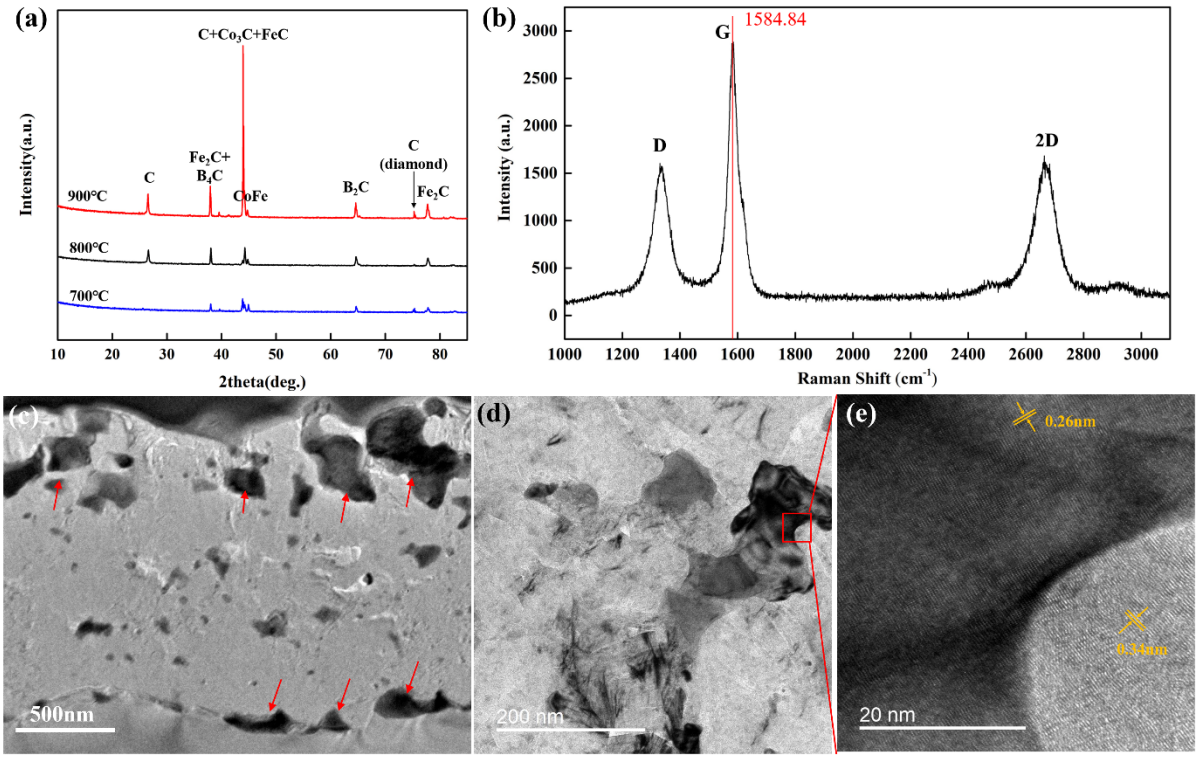

Figure 2 (a) X-ray diffractograms of reaction zone of diamond with 150nm FeCoB layers annealed under 700°C, 800°C, and 900°C for 30 min. Accelerated reaction occurs at temperatures greater than 800°C. (b) Raman spectrum of a diamond substrate reacted with a 150nm FeCoB layer at 800°C for 90 min; (c) TEM image of the diffusional interaction layer between 150nm FeCoB and diamond under 800°C for 90 min. Red arrows indicate islands of dark contrast that inhabit the interface between diamond and the reaction zone. (d) Higher magnification TEM image of regions of dark contrast observed in c. (e) shows the corresponding High resolution TEM image.

A significant challenge in translating the utility of solid-state etchants into scalable frameworks for creating micro/nanostructured diamond surfaces is in achieving surfaces of controllable topographical quality. Localizing the interaction between diamond and TM within the interaction zone is key. EDS mapping and line scan under TEM were performed to characterize the compositional gradients within the interaction zone (Figure 3). The islands of dark contrast are found to be rich in Fe and Co – the higher Z atoms are strong scatterers of electrons. The matrix is essentially carbon, which was converted into the sp^2 form from the diamond (Figure 3a). The line scans in Figure 3b illustrate how the regions with a significant Fe and Co content are poor in C, compared to the surrounding matrix (of lighter bright field contrast in the TEM). Furthermore, the C content in the metal rich islands declines as we move from the diamond interface, further into the graphitized interaction layer. The dispersion of the metal rich regions into the C matrix in the interaction zone reveals a fragmentation of the solid-state etchant during the progressive conversion of diamond into sp^2 carbon and its transport through the FeCoB. Moreover, the EDS did not defect significant oxygen or nitrogen. This result, in conjunction

with XRD and Raman spectroscopy results, indicate a minor role of any residual air ($<1\times10^{-6}$ mBar) in the diamond/TM interaction. These experimental insights are schematized in Figure 4.

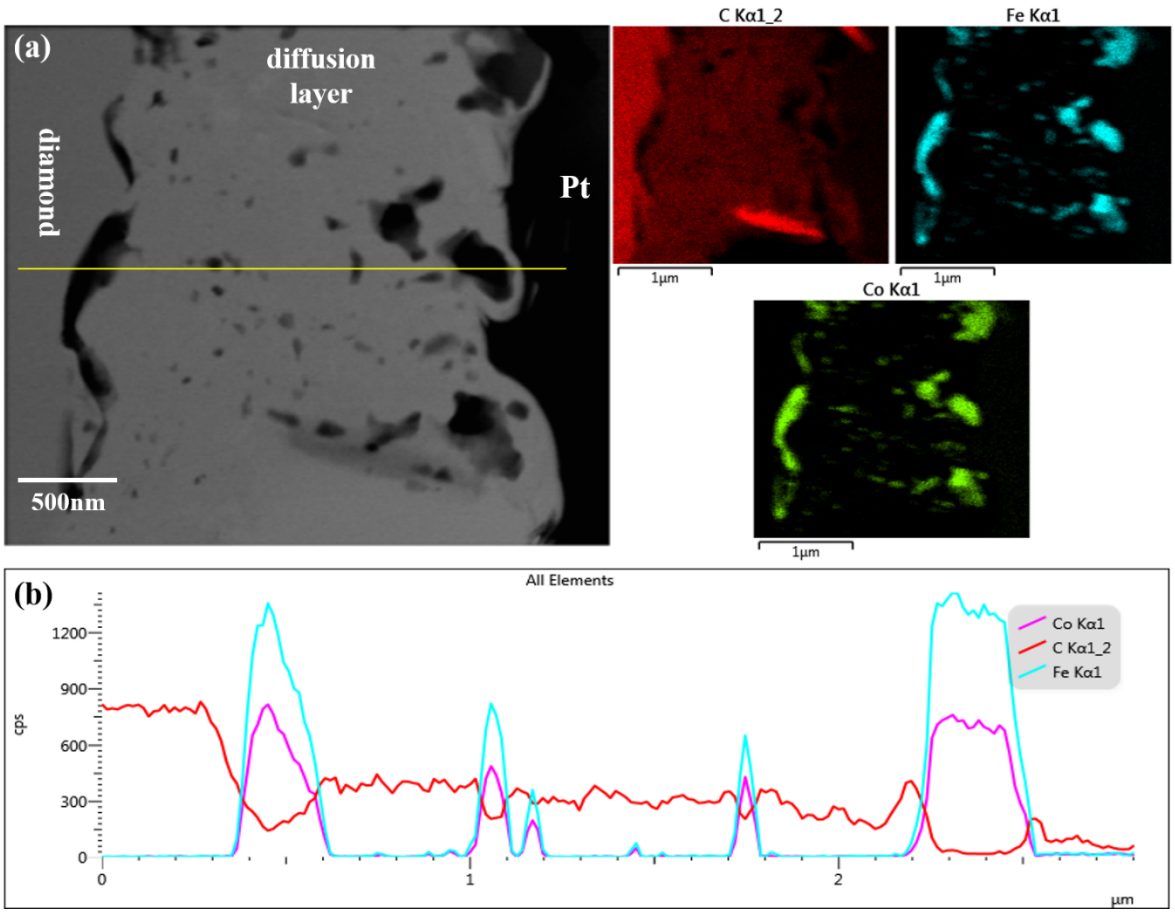

Figure 3. EDS map and line scan of the interface between the diamond substrate and 150 nm FeCoB annealed after heat treatment at 800℃ for 90 min. (a) Bright field TEM image of the diffusion layer and the corresponding element distribution and C, Fe, and Co. (b) Element distribution of C, Fe, and Co along the yellow line in (a).

A temperature of >700℃ is required to trigger the reaction between the diamond and the TM etchant (Figure 4a). The carbon bonds in diamond lattice are broken to release free carbon atoms diffusing into the contacting FeCoB lattice. This increases the carbon density in the FeCoB grains (Figure 4b)[29, 36]. After the carbon density is saturated, the carbon segregate at the FeCoB grain boundaries and contribute to the fragmentation of the FeCoB (Figure 4c),

which was initially a continuous and integral layer on the diamond. The C is then progressively converted into the sp^2 hybridized carbon layer, which forms the matrix of the interaction layer. This conversion also involves the formation of carbides, as revealed in the XRD characterization in Figure 2a. As the reaction proceeds the interaction layer grows and C is progressively removed from the underlying diamond. The role of the TM/diamond interface is key, and this also explains the insensitivity of the etching to the thickness of the TM layer that is deposited atop the diamond (Figure S4). The fragmentation of the FeCoB layer leads to the dispersal of the nanocrystals within the sp^2 matrix (Figure 4d). The disruption of the etchant in this manner is detrimental to the overall process and contributes to the progressive loss of specificity in the diamond removal. However, FeCoB allows for efficient removal of diamond in a manner that is significantly more accelerated than that with just Fe or Co (Figure 1d). Note that the reaction layer is amenable to solvothermal removal, which allows for inheriting the suitably structured diamond as shown in Figure 1a and confirmed by the Raman spectrum in Figure S5. A potential pathway for inheriting the efficient diamond removal and improving the specificity of the material removal emerges by optimizing the composition of the composition and microstructure of the FeCoB. If the fragmentation of the etchant layer during the diamond's conversion to sp^2 carbon can be suppressed, the TM layer can transform and remove diamond in a stable and localized manner.

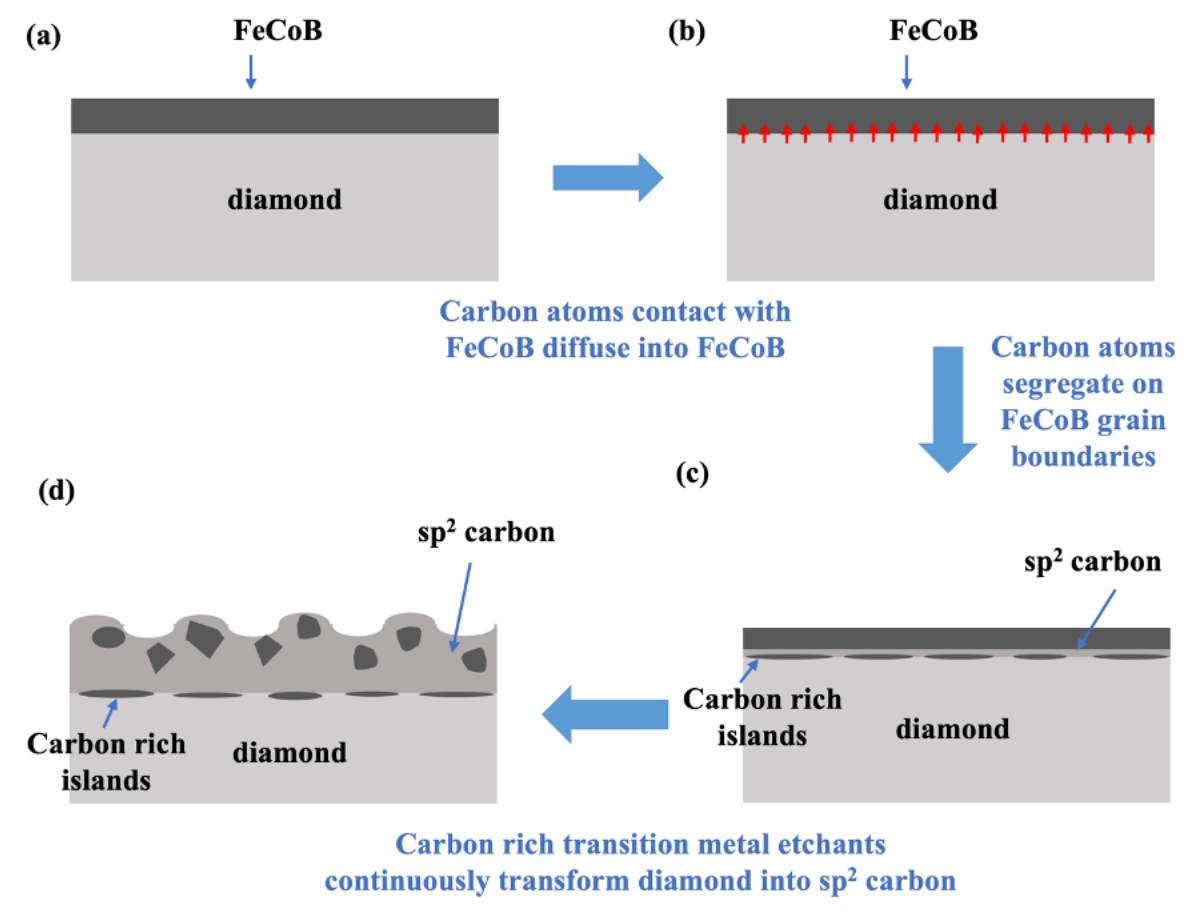

Figure 4. Schematic illustration of the diffusional reaction process at a diamond-FeCoB interface.

4. Conclusions:

Spatially selective diffusion of C across diamond-FeCoB interfaces enables solid-state patterning of polycrystalline diamond substrates. Lithographically patterned transition metal coatings accelerate the removal of C from diamond at temperatures >800°C. Furthermore, the material removal rate with FeCoB exceeds that possible with just Fe or Co, which indicates the role of B in accelerating the interaction. This approach is exploited at the micrometer-scale to enable topographical texturing of diamond. The stability of the diamond-transition metal interface is key to preserving the spatial selectivity of the material removal. Electron microscopy of the reaction zone reveals the conversion of sp^3 to sp^2 carbon. The loss of

selectivity in material removal is primarily due to the disruption of the integrity of the FeCoB layer during the progressive material removal. The reaction products in the diffusional interaction layer of diamond and FeCoB alloy are primarily composed of sp^2 carbon along with metal rich islands, including metal carbides and alloys. Optimizing the composition of multicomponent, transition metal based solid state etchants to increase their stability against C segregation driven rupture will hold the key to achieving high rates of etching, while preserving the spatial selectivity of the material removal.

Acknowledgements

Support from the II-VI Foundation Block Gift program and the National Science Foundation (1921842) are gratefully acknowledged.

References:

[1] S. Basu, M.R. Shankar, Spatial confinement-induced switchover in microstructure evolution during severe plastic deformation at micrometer length scales, Acta Materialia 79 (2014) 146-158.
[2] Z.J. Yuan, M. Zhou, S. Dong, Effect of diamond tool sharpness on minimum cutting thickness and cutting surface integrity in ultraprecision machining, Journal of Materials Processing Technology 62(4) (1996) 327-330.
[3] T.D.B. Jacobs, R.W. Carpick, Nanoscale wear as a stress-assisted chemical reaction, Nature nanotechnology 8(2) (2013) 108-112.
[4] R.P. Dias, I.F. Silvera, Observation of the Wigner-Huntington transition to metallic hydrogen, Science 355(6326) (2017) 715.
[5] S.J. Bull, A. Matthews, Diamond for wear and corrosion applications, Diamond and Related Materials 1(10) (1992) 1049-1064.
[6] T.V. Kononenko, D.N. Sovyk, P.A. Pivovarov, V.S. Pavelyev, A.V. Mezhenin, K.V. Cherepanov, M.S. Komlenok, V.R. Sorochenko, A.A. Khomich, V.P. Pashinin, E.E. Ashkinazi, V.G. Ralchenko, V.I. Konov, Fabrication of diamond diffractive optics for powerful CO2 lasers via replication of laser microstructures on silicon template, Diamond and Related Materials 101 (2020) 107656.
[7] V. Damle, K. Wu, O. De Luca, N. Ortí-Casañ, N. Norouzi, A. Morita, J. de Vries, H. Kaper, I.S. Zuhorn, U. Eisel, D.E.P. Vanpoucke, P. Rudolf, R. Schirhagl, Influence of diamond crystal orientation on the interaction with biological matter, Carbon 162 (2020) 1-12.
[8] J. Fu, T.F. Zhu, M.H. Zhang, X. Zhang, F.N. Li, Z.C. Liu, G.A. Denu, Y.F. Wang, D. Zhao, G.Q. Shao, X.H. Chang, W. Wang, J.W. Zhang, H.X. Wang, J.J. Wang, X. Hou, Fabrication of single crystal diamond microchannels for micro-electromechanical systems, Diamond and Related Materials 80 (2017) 64-68.
[9] S. Li, J.-P. Chou, J. Wei, M. Sun, A. Hu, A. Gali, Oxygenated (113) diamond surface for nitrogen-vacancy quantum sensors with preferential alignment and long coherence time from first principles, Carbon 145 (2019) 273-280.
[10] Y. Tao, J.M. Boss, B.A. Moores, C.L. Degen, Single-crystal diamond nanomechanical resonators with quality factors exceeding one million, Nature Communications 5(1) (2014) 3638.
[11] X. Zhu, S. Saito, A. Kemp, K. Kakuyanagi, S.-i. Karimoto, H. Nakano, W.J. Munro, Y. Tokura, M.S. Everitt, K. Nemoto, M. Kasu, N. Mizuochi, K. Semba, Coherent coupling of a superconducting flux qubit to an electron spin ensemble in diamond, Nature 478(7368) (2011) 221-224.
[12] P. Maletinsky, S. Hong, M.S. Grinolds, B. Hausmann, M.D. Lukin, R.L. Walsworth, M. Loncar, A. Yacoby, A robust scanning diamond sensor for nanoscale imaging with single nitrogen-vacancy centres, Nature Nanotechnology 7(5) (2012) 320-324.
[13] Z. Zhang, H. Wu, L. Sang, J. Huang, Y. Takahashi, L. Wang, M. Imura, S. Koizumi, Y. Koide, M. Liao, Single-crystal diamond microelectromechanical resonator integrated with a magneto-strictive galfenol film for magnetic sensing, Carbon 152 (2019) 788-795.
[14] I. Aharonovich, E. Neu, Diamond Nanophotonics, Advanced Optical Materials 2(10) (2014) 911-928.

[15] L. Xie, T.X. Zhou, R.J. Stöhr, A. Yacoby, Crystallographic Orientation Dependent Reactive Ion Etching in Single Crystal Diamond, Advanced Materials 30(11) (2018) 1705501.
[16] Y. Ando, Y. Nishibayashi, K. Kobashi, T. Hirao, K. Oura, Smooth and high-rate reactive ion etching of diamond, Diamond and Related Materials 11(3) (2002) 824-827.
[17] B. Khanaliloo, M. Mitchell, A.C. Hryciw, P.E. Barclay, High-Q/V Monolithic Diamond Microdisks Fabricated with Quasi-isotropic Etching, Nano Letters 15(8) (2015) 5131-5136.
[18] J. Enlund, J. Isberg, M. Karlsson, F. Nikolajeff, J. Olsson, D.J. Twitchen, Anisotropic dry etching of boron doped single crystal CVD diamond, Carbon 43(9) (2005) 1839-1842.
[19] M.J. Burek, N.P. de Leon, B.J. Shields, B.J.M. Hausmann, Y. Chu, Q. Quan, A.S. Zibrov, H. Park, M.D. Lukin, M. Lončar, Free-Standing Mechanical and Photonic Nanostructures in Single-Crystal Diamond, Nano Letters 12(12) (2012) 6084-6089.
[20] A.A. Martin, A. Bahm, J. Bishop, I. Aharonovich, M. Toth, Dynamic Pattern Formation in Electron-Beam-Induced Etching, Physical Review Letters 115(25) (2015) 255501.
[21] J. Bishop, M. Fronzi, C. Elbadawi, V. Nikam, J. Pritchard, J.E. Fröch, N.M.H. Duong, M.J. Ford, I. Aharonovich, C.J. Lobo, M. Toth, Deterministic Nanopatterning of Diamond Using Electron Beams, ACS Nano 12(3) (2018) 2873-2882.
[22] A.A. Martin, M. Toth, I. Aharonovich, Subtractive 3D Printing of Optically Active Diamond Structures, Scientific Reports 4(1) (2014) 5022.
[23] T.V. Kononenko, V.V. Kononenko, V.I. Konov, S.M. Pimenov, S.V. Garnov, A.V. Tishchenko, A.M. Prokhorov, A.V. Khomich, Formation of antireflective surface structures on diamond films by laser patterning, Applied Physics A 68(1) (1999) 99-102.
[24] J. Riedrich-Möller, L. Kipfstuhl, C. Hepp, E. Neu, C. Pauly, F. Mücklich, A. Baur, M. Wandt, S. Wolff, M. Fischer, S. Gsell, M. Schreck, C. Becher, One- and two-dimensional photonic crystal microcavities in single crystal diamond, Nature Nanotechnology 7(1) (2012) 69-74.
[25] Y. Zheng, H. Ye, J. Liu, J. Wei, L. Chen, C. Li, Surface morphology evolution of a polycrystalline diamond by inductively coupled plasma reactive ion etching (ICP-RIE), Materials Letters 253 (2019) 276-280.
[26] S.J. Zhang, S. To, G.Q. Zhang, Diamond tool wear in ultra-precision machining, The International Journal of Advanced Manufacturing Technology 88(1) (2017) 613-641.
[27] J. Wang, G. Zhang, N. Chen, M. Zhou, Y. Chen, A review of tool wear mechanism and suppression method in diamond turning of ferrous materials, The International Journal of Advanced Manufacturing Technology 113(11) (2021) 3027-3055.
[28] E. Paul, C.J. Evans, A. Mangamelli, M.L. McGlauflin, R.S. Polvani, Chemical aspects of tool wear in single point diamond turning, Precision Engineering 18(1) (1996) 4-19.
[29] L. Zou, J. Yin, Y. Huang, M. Zhou, Essential causes for tool wear of single crystal diamond in ultra-precision cutting of ferrous metals, Diamond and Related Materials 86 (2018) 29-40.
[30] M.S. Uddin, K.H.W. Seah, M. Rahman, X.P. Li, K. Liu, Performance of single crystal diamond tools in ductile mode cutting of silicon, Journal of Materials Processing Technology 185(1) (2007) 24-30.
[31] N. Yang, W. Huang, D. Lei, Control of nanoscale material removal in diamond polishing by using iron at low temperature, Journal of Materials Processing Technology 278 (2020) 116521.
[32] A. Kubota, S. Nagae, S. Motoyama, M. Touge, Two-step polishing technique for single

crystal diamond (100) substrate utilizing a chemical reaction with iron plate, Diamond and Related Materials 60 (2015) 75-80.
[33] A. Kubota, S. Motoyama, M. Touge, Surface smoothing of a polycrystalline diamond using an iron plate-H2O2 chemical reaction, Diamond and Related Materials 69 (2016) 96-101.
[34] M. Nagai, K. Nakanishi, H. Takahashi, H. Kato, T. Makino, S. Yamasaki, T. Matsumoto, T. Inokuma, N. Tokuda, Anisotropic diamond etching through thermochemical reaction between Ni and diamond in high-temperature water vapour, Scientific Reports 8(1) (2018) 6687.
[35] Y. Kato, H. Kawashima, T. Makino, M. Ogura, A. Traoré, N. Ozawa, S. Yamasaki, Estimation of Inductively Coupled Plasma Etching Damage of Boron-Doped Diamond Using X-Ray Photoelectron Spectroscopy, physica status solidi (a) 214(11) (2017) 1700233.
[36] S. Zenkin, A. Gaydaychuk, V. Okhotnikov, S. Linnik, CVD diamond interaction with Fe at elevated temperatures, Materials 11(12) (2018) 2505.
[37] S. Cui, A.S. Greenspon, K. Ohno, B.A. Myers, A.C.B. Jayich, D.D. Awschalom, E.L. Hu, Reduced Plasma-Induced Damage to Near-Surface Nitrogen-Vacancy Centers in Diamond, Nano Letters 15(5) (2015) 2887-2891.
[38] J. Wang, L. Wan, J. Chen, J. Yan, Anisotropy of synthetic diamond in catalytic etching using iron powder, Applied Surface Science 346 (2015) 388-393.
[39] V.G. Ralchenko, T.V. Kononenko, S.M. Pimenov, N.V. Chernenko, E.N. Loubnin, V.Y. Armeyev, A.Y. Zlobin, Catalytic interaction of Fe, Ni and Pt with diamond films: patterning applications, Diamond and Related Materials 2(5) (1993) 904-909.
[40] A. Yang, H. Imrane, J. Lou, J. Kirkland, C. Vittoria, N. Sun, V.G. Harris, Effects of boron addition to the atomic structure and soft magnetic properties of FeCoB films, Journal of Applied Physics 103(7) (2008) 07E736.
[41] C.L. Platt, N.K. Minor, T.J. Klemmer, Magnetic and structural properties of FeCoB thin films, IEEE Transactions on Magnetics 37(4) (2001) 2302-2304.
[42] S.J. Chae, F. Güneş, K.K. Kim, E.S. Kim, G.H. Han, S.M. Kim, H.-J. Shin, S.-M. Yoon, J.-Y. Choi, M.H. Park, C.W. Yang, D. Pribat, Y.H. Lee, Synthesis of Large-Area Graphene Layers on Poly-Nickel Substrate by Chemical Vapor Deposition: Wrinkle Formation, Advanced Materials 21(22) (2009) 2328-2333.
[43] D.L. Silva, J.L.E. Campos, T.F.D. Fernandes, J.N. Rocha, L.R.P. Machado, E.M. Soares, D.R. Miquita, H. Miranda, C. Rabelo, O.P. Vilela Neto, A. Jorio, L.G. Cançado, Raman spectroscopy analysis of number of layers in mass-produced graphene flakes, Carbon 161 (2020) 181-189.
[44] Z. Ni, Y. Wang, T. Yu, Z. Shen, Raman spectroscopy and imaging of graphene, Nano Research 1(4) (2008) 273-291.
[45] J.L. Qi, J.H. Lin, X. Wang, J.L. Guo, L.F. Xue, J.C. Feng, W.-D. Fei, Low resistance VFG-Microporous hybrid Al-based electrodes for supercapacitors, Nano Energy 26 (2016) 657-667.
[46] D.H. Seo, Z.J. Han, S. Kumar, K. Ostrikov, Structure-Controlled, Vertical Graphene-Based, Binder-Free Electrodes from Plasma-Reformed Butter Enhance Supercapacitor Performance, Advanced Energy Materials 3(10) (2013) 1316-1323.